PROBA2 LYRA Occultations: Thermospheric Temperature and Composition, Sensitivity to EUV Forcing and Comparisons with Mars

Edward M. B. Thiemann[1], Marie Dominique[2]

[1]Laboratory for Atmospheric and Space Physics, University of Colorado Boulder
[2]Solar-Terrestrial Centre of Excellence, Royal Observatory of Belgium

Key Points:

- Temperature and composition from 150-350 km from 2010-2017 are presented.
- Dusk temperatures are markedly cooler than MSIS predictions.
- Mars exospheric temperature is half as sensitive to EUV variability as that of Earth.

Corresponding author: E. M. B. Thiemann, thiemann@lasp.colorado.edu

Abstract

A method is presented for retrieving temperature and composition from 150-350 km in Earth's thermosphere using total number density measurements made via EUV solar occultations by the PROBA2/LYRA instrument. Systematic and random uncertainties are calculated and found to be less than 5% for the temperature measurements and 5-20% for the composition measurements. Regression coefficients relating both temperature and the $[O]/[N_2]$ abundance ratio with EUV irradiance at 150, 275 and 350 km are reported. Additionally, it is shown that the altitude where [O] equals $[N_2]$ decreases with increasing solar EUV irradiance, an effect attributed to thermal expansion. Temperatures from 2010 to 2017 are compared with estimates from the MSIS empirical model and show good agreement at the dawn terminator but LYRA is markedly cooler at the dusk terminator, with the MSIS-LYRA temperature difference increasing with solar activity. Anthropogenic cooling can explain this discrepancy at periods of lower solar activity, but the divergence of temperature with increasing solar activity remains unexplained. LYRA measurements of the exospheric sensitivity to EUV irradiance are compared with contemporaneous measurements made at Mars, showing that the exospheric temperature at Mars is approximately half as sensitive to EUV variability as that of Earth.

1 Introduction

The Earth's thermosphere, the upper region of its neutral atmosphere, extends from the temperature minimum at the mesopause (85-100 km; Xu et al. (2007)) to geospace. Spanning the regions of both the ionosphere and Low Earth Orbit (LEO), the thermosphere and its state have important implications for space weather (Schunk & Sojka, 1996). Photochemical and dynamical processes in the thermosphere change its temperature, density and composition, directly influencing satellite drag and trans-ionospheric electromagnetic propagation. Geomagnetic storms provide perhaps the most dramatic example of the interplay between the magnetosphere, thermosphere and ionosphere, and the resulting impact on space weather (e.g. Mayr and Volland (1973); Fuller-Rowell et al. (1994)). Currents induced in the magnetosphere cause intense heating in the lower thermosphere, driving an upwelling of N_2 rich air. Satellite drag increases significantly over the poles, resulting in the temporary or even permanent loss of satellite trajectory knowledge. In the ionosphere, the increased N_2 abundance depletes the local plasma density due to the faster recombination rate of N_2 ions relative to O ions (e.g. Wang et al. (2010)), impacting trans-ionospheric communications signals.

The region of the thermosphere between 150 and 300 km is of particular scientific importance. It is within this region that the thermosphere's temperature increases sharply, due primarily to the absorption of solar Extreme Ultraviolet (EUV) radiation except for near the auroral zone, where geomagnetic heating becomes important. As such, the thermal balance of the upper atmosphere, and ultimately the exospheric temperature, is largely the result of processes occurring between 150 and 300 km (R. G. Roble et al., 1987). The absorption of EUV radiation also causes the plasma density to peak within this altitude range (R. G. Roble, 1995). Additionally, it is within the 150-300 km range that substantial coupling between the lower and upper regions of Earth's atmosphere are expected to occur (Vadas, 2007; Yiğit & Medvedev, 2009; Oberheide et al., 2011; Miyoshi et al., 2015). Gravity waves and tides originating in the lower atmosphere propagate upwards and deposit energy and momentum in the lower and middle thermosphere, causing variability at short time-scales and influencing the circulation and thermal balance globally. Despite its importance, measurements targeting neutral density and composition across the 150 to 300 km altitude range have been limited because of the inherent difficulty in measuring neutral species at these altitudes directly.

Figure 1 shows a chart of neutral density, temperature and composition measurements since 1973 as a function of altitude and time. The Atmospheric Explorer E (AE-

E) and Dynamics Explorer (DE) missions measured neutral species in-situ by mass spectrometry (Nier et al., 1973; Carignan et al., 1981);. These spacecraft had highly elliptical orbits, allowing a range of altitudes to be sampled during each orbit. The Challenging Minisatellite Payload (CHAMP; Bruinsma and Biancale (2003)), Gravity Recovery and Climate Experiment (GRACE; Sutton et al. (2007)) and Gravity Field and Steady-State Ocean Circulation Explorer (GOCE; Bruinsma et al. (2014)) missions measured total mass density in-situ using precision accelerometers. These spacecrafts' orbits were more circular, restricting the sampling to a nearly fixed altitude over a single orbit, which decreased as the orbits decayed. The Thermosphere, Ionosphere, Mesosphere Energetics and Dynamics (TIMED) Global Ultraviolet Imager (GUVI) measurements shown in Figure 1 were made by limb scans of atmospheric airglow (Meier et al., 2015). These limb scans ceased in 2008 due to a mechanism failure, while TIMED/GUVI continues to make measurements of column integrated airglow (without altitude resolution) up to the time of this writing. The GOLD mission measures profiles of O_2 density using stellar occultations (shown in pink) and column integrated airglow measurements of density and composition near the altitude of the airglow peak (150-180 km).

The remaining measurements in Figure 1 are from ultraviolet (UV) solar occultations. UV solar occultations served as an early workhorse for characterizing upper atmospheric density and composition (preceding the measurements shown in Figure 1), where researchers exploited the fact that much of the UV spectrum is strongly absorbed by the major species of the upper atmosphere (see R. G. Roble and Hays (1972) and references therein). However, solar occultation specific instruments for observing the thermosphere have not flown in recent decades, even as both the quantity and quality of space-borne solar UV instrumentation have increased substantially, and solar occultation measurements shown in Figure 1 are "bonus" measurements made by instruments intended to study the Sun. Between 1983 and 2005, solar occultations of O_2 density were made by the Ultraviolet Spectrometer and Polarimeter (UVSP) onboard the Solar Maximum Mission (SMM) and the Solar Ultraviolet Spectral Irradiance Monitor (SUSIM) onboard the Upper Atmosphere Research Satellite (Aikin et al., 1993; Lumpe et al., 2007). More recently, Thiemann et al. (2017) demonstrated the utility of modern solar EUV instruments for thermospheric solar occultations by using solar EUV measurements made by the Large Yield Radiometer (LYRA) instrument onboard the European Space Agency (ESA) Project for OnBoard Autonomy 2 (PROBA2) satellite to measure total number density between 150 and 350 km.

This paper builds on the work of Thiemann et al. (2017) by extending the retrievals of the LYRA solar occultation measurements to include thermospheric temperature and composition, and the primary objective of this paper is to report the methods and the uncertainties of the retrieval. Section 2 describes the data, retrieval methods and associated uncertainties in detail. These new data are used to establish the dependence of thermospheric temperature and composition on solar EUV forcing at various altitudes in Section 3. Section 3 also compares the LYRA measurements with predictions by the NRLMSISE-00 model (Picone et al. (2002), hereafter MSIS). These results are discussed in Section 4 and main conclusions are stated in Section 5.

2 Data and Methods

Solar occultation measurements are made using the LYRA instrument onboard PROBA2 launched by ESA in 2009. PROBA2 flies in a retrograde Sun-synchronous orbit ($\sim$700 km of altitude, 98^o of inclination), which generates brief occultations for three months each year (from early November through early February) when the spacecraft enters eclipse at the dawn terminator, and exits it at the dusk terminator. At these moments, LYRA can observe the Sun through the Earth's atmosphere, and the detected signal is attenuated by an amount that depends on the altitude, the channel spectral response and the atmospheric composition. The mean observation latitude varies between 45^o and 65^o (25^o

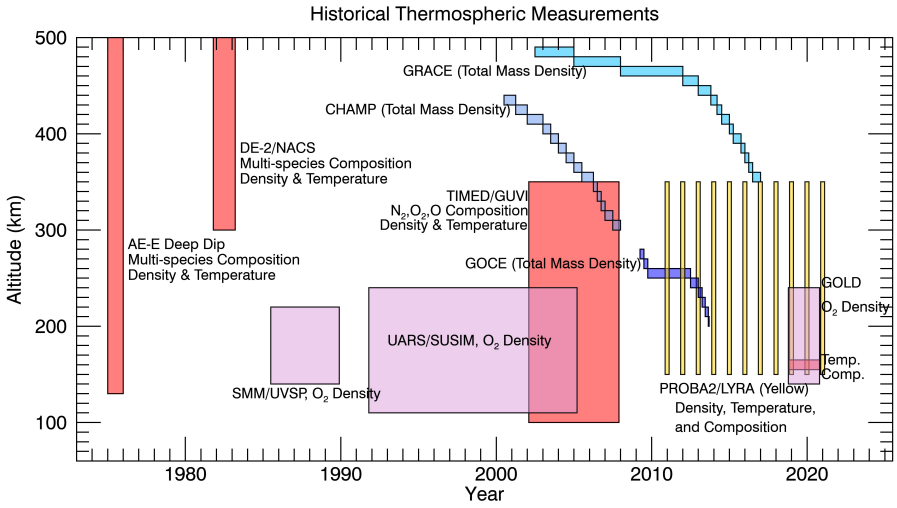

Figure 1. Chart of measurements of thermospheric neutral species over time and altitude range sampled. Measurements by LYRA, the topic of this paper, are shown in yellow.

and 50^o) North over an occultation season at the Dawn (Dusk) terminator as illustrated in Figure 2 of Thiemann et al. (2017). Simulations show that the measurements are fairly localized in the line of sight direction, with 70% of the observed column density located within 400 to 475 km of the terminator, which corresponds with ∼15 minutes of solar local time.

LYRA monitors the full-disk solar irradiance at high cadence (nominally 20 Hz, resampled to 1 Hz for occultations) in four broad channels: Lyman-alpha (120-123 nm), Herzberg (190-222 nm), Al (.1-80 nm), and Zr (.1-20 nm), and three redundant units: The primary unit, used for monitoring the Sun in a quasi-uninterrupted way; the back-up unit, used for special observation campaigns including solar occultations because of its more accurate calibration; and a third unit, reserved for calibration purposes. Prior to November 2017, the back-up unit nominally made occultation observations for a single orbit per day during eclipse seasons. Densities were retrieved from these data by Thiemann et al. (2017) and made publicly available. These data are the starting point of this paper (see Section 5 for data access details). Beginning in November 2017 through the present, LYRA began making occultation observations with the back-up unit every orbit during eclipse season. The higher cadence data have yet to be processed for atmospheric densities, and analysis of these higher cadence data are planned for a future study.

The spectral response of the instrument was measured prior to launch during calibration campaigns at the Physikalisch-Technische Bundesanstalt (PTB) Berlin Electron Storage Ring Society for Synchrotron Radiation (BESSY) II synchrotron as reported in BenMoussa et al. (2009). However, continuous solar exposure has caused severe degradation of the primary unit that significantly modifies the instrument spectral response, which is suspected to the result of the formation of C layer on the optics (BenMoussa et al., 2013). The backup unit also shows signs of degradation, but to a lesser extent. The Zr channel seems to be the least sensitive to degradation, although, the signal acquired by this channel has decreased by approximately 30% between January, 2010 and April, 2017. The reduced Zr channel degradation can be explained by the fact that this channel is mostly sensitive to short wavelengths (below 20 nm), where the absorption cross-section of the C contaminant is smaller. However, the presence of the C contam-

inant will bias the atmospheric densities deduced from the absorption by the Earth atmosphere and Thiemann et al. (2017) established a series of correction factors for the retrieved densities to account for the instrument degradation.

Thermospheric temperature and composition are retrieved from the LYRA total number density profiles described in Thiemann et al. (2017). These LYRA density data consist of summed [O] and [N_2] from 150 - 350 km derived from the LYRA Zr channel. The similarity of the O and N_2 absorption cross-sections over the LYRA Zr channel bandpass result in photon absorption by an O atom being indistinguishable from that by an N_2 molecule. In principle, including measurements from the Al channel in the density retrieval algorithm would provide the additional constraint needed to distinguish [O] from [N_2]. However, this channel has suffered from uncorrected degradation and its response function is presently ill-determined, necessitating an alternate approach for determining atmospheric composition and ultimately temperature from the LYRA [O]+[N_2] profiles.

The approach presented here leverages the well-established understanding of thermospheric structure in lieu of additional observations to provide the necessary constraints to derive temperature and composition from the LYRA [O]+[N_2] profiles. Namely, the temperature as a function of altitude (z) generally follows the relation first presented by Bates (1959),

$$T(z) = T_{exo}\left[1 - a\exp\left(-\tau\zeta\right)\right], \tag{1}$$

where T_{exo} is the exospheric temperature, ζ is the geopotential height, and a and τ are constants. The latter three terms are defined as

$$\zeta = \int_{z_0}^{z} \frac{g(z)}{g(z_0)} dz \tag{2}$$

$$a = 1 - \frac{T(z_0)}{T_{exo}} \tag{3}$$

$$\tau = \frac{1}{T_{exo} - T(z_0)} \left(\frac{dT}{dz}\right)_{z=z_0} \tag{4}$$

where g is gravity and z_0 is some reference altitude. Assuming diffusive equilibrium, vertical density structure for species s, n_s, is governed by (e.g. Schunk and Nagy (2009))

$$n_s(z) = n_s(z_1)\frac{T(z_1)}{T(z)}\exp\left(-\int_{z_1}^{z}\frac{m_s g}{k_B T}dz'\right), \tag{5}$$

where z_1 is some reference altitude (which can differ from z_0) and k_B is Boltzmann's constant. Strictly speaking, equation (5) only holds for inert gases such as N_2. However, agreement was found (not shown here) to be within 1% above 150 km between [O] profiles using equation (5) and those from the NRL-MSISE-00 empirical model (Picone et al. (2002); herafter MSIS) for the LYRA observing locations and times. Below 150 km, photochemical production of [O] becomes increasingly important, causing the approximation of equation (5) to break down. Equation (5) is fit against the LYRA [O] +[N_2] measurements (constraining T with equation (1)) using the Levenberg-Marquardt non-linear least-squares fitting method (e.g. Press et al. (2007)), while forcing T_{exo}, a, τ, $n_o(z_1)$, $n_{N2}(z_1)$ to remain within values physically consistent with the [O]+[N_2] profiles as discussed below.

Initial values of T_{exo}, $n_o(z_1)$ and $n_{N2}(z_1)$ are estimated from the measured [O]+[N_2] profiles. These profiles typically extend to 350 km near solar minimum (and above 400 km near solar maximum). At these upper altitudes, [O] is expected to be the major species

and the temperature is nearly or completely isothermal. As such, an exponential fit of the [O]+[N_2] profiles at the highest observed altitudes provides an initial estimate of [$O(z)$] at high altitudes, and exospheric temperature (T_{exo}) is estimated from the fitted scale height, H, according to $H = k_B T/m_o g$. Further, the difference of the measured [$O(z)$]+[$N_2(z)$] and fitted [$O(z)$] values, provides an initial estimate of [$N_2(z)$]. Initial estimates of $n_o(z_1)$ and $n_{N2}(z_1)$ are found directly from the initial [$N_2(z)$] and [$O(z)$] estimates at an altitude where the temperature is nearly isothermal and the signal to noise ratio (SNR) is relatively large. It was found through trial and error that [N_2] values of 2×10^8 cm^{-3} provide a good balance between sufficient SNR and isothermality. As such, z_1 is defined where $n_{N2}(z_1) = 2 \times 10^8$ cm^{-3} from the initial [$N_2(z)$] approximation. Figure 2 (a) shows an example [O]+[N_2] measured profile with a black curve, and initial estimates of the [O] and [N_2] profiles with red-dashed and blue-dotted curves, respectively. The corresponding initial estimates of $n_o(z_1)$ and $n_{N2}(z_1)$ are also shown.

Initial values of a and τ are estimated using linear fits between these parameters and T_{exo} found using MSIS for all LYRA observing times and locations. Figures 2 (b) and(c) show how a and τ vary as functions of T_{exo}, with the corresponding first-order linear fits overplotted. $\tau(T_{exo})$ is found to have a markedly more shallow slope for values of T_{exo} above 950 K, requiring two separate fits to best represent the functional relationship. The fit coefficients and standard deviations (σ) are reported in the figures.

Prior to retrieving temperature and composition, the LYRA [O]+[N_2] profiles undergo minor corrections suggested in Thiemann et al. (2017) but not applied to the publicly available data. First, correction factors for optical degradation in the LYRA instrument reported in Table 1 of Thiemann et al. (2017) are applied to the profiles. Second, the retrieval systematic bias is removed using the error profile reported in Figure 2d of Thiemann et al. (2017). Third, latitudinal variability is corrected as follows: For a typical LYRA solar occultation profile, the observing latitudes varies by approximately 10^o between 150 and 350 km altitude. This latitudinal variation must be corrected for prior to fitting the LYRA data to equation (5) because equation (5) assumes the atmospheric density profile is perfectly vertical. MSIS is used to calculate correction factors at each altitude by first predicting [O]+[N_2] profiles at the exact LYRA observing latitudes and altitudes ($n_{MSIS,true}(z)$) and at the mean LYRA observing latitude ($n_{MSIS,mean}(z)$). The measured LYRA profiles are corrected to the corresponding fixed mean latitude by multiplying them by $n_{MSIS,mean}(z)/n_{MSIS,true}(z)$. An example of this correction profile for 30 December 2013 is shown in Figure 2(d).

The IDL Levenberg-Marquardt solver mpfit.pro is used to find the optimal values of T_{exo}, $n_o(z_1)$, $n_{N2}(z_1)$,a and τ by fitting equation (5) (which, in turn, depends on equation (1)) to the latitude-corrected LYRA [$O(z)$]+[$N_2(z)$] measurements. The fit is initialized using the initial values described above. T_{exo} is allowed to range between 0.9 and 1.1 of its initial value. $n_o(z_1)$ and $n_{N2}(z_1)$ are allowed to range between 0.5 and 1.5 of their initial values. And a and τ are allowed to vary by their 1-σ fit-error values (reported in Figure 2). The range of allowed variability for the fit parameters was optimized by trial and error to minimize the random uncertainty and systematic error of the retrieval algorithm.

The random uncertainty and systematic error of the temperature and composition retrieval algorithm are quantified by generating composition-resolved density and temperature profiles for each LYRA observing latitude and time. Synthetic LYRA measurements are found by summing the MSIS [O] and [N_2] estimates and adding random noise corresponding to the expected measurement random uncertainty at each altitude. Temperature and composition are retrieved from these synthetic measurements using the methods described above. The retrieved T, [O] and [N_2] profiles are compared with those predicted by MSIS and the mean fractional difference defines the systematic error while the standard deviation of the fractional difference defines the random uncertainty of the retrieval. The errors and uncertainties are reported in Figure 3. The temperature random

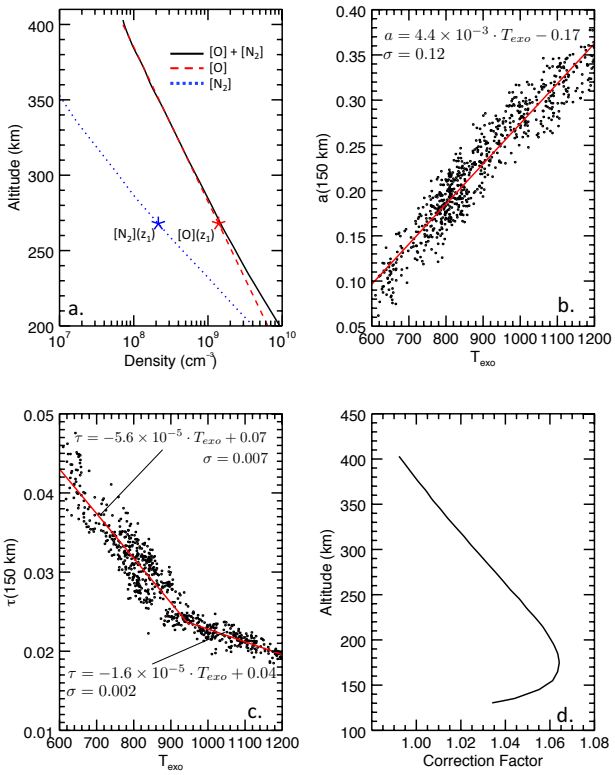

Figure 2. Estimates of constraints on fitted parameters. (a) An exponential fit (red-dashed curve) to the [O]+[N_2] LYRA measurements (black curve) provides an estimate of the [O] profile at high altitudes, and T_{exo} can be derived from the fitted scale-height. The difference of the black and red-dashed curves provides an estimate of the [N_2] profile at high altitudes. The asterisks indicate estimates of $n_o(z_1)$ and $n_{N2}(z_1)$ used to fit equation (5) to the [O]+[N_2] measurements. (b) Scatter-plot and linear fit of a and T_{exo} derived from MSIS for the LYRA observing locations and times. (c) Scatter-plot and linear fit of τ and T_{exo} derived from MSIS for the LYRA observing locations and times. (d) Example correction factor for verticalizing [O]+[N_2] profile measured on 30-Dec-2013.

uncertainty ranges between 2 and 5 %, while the temperature systematic error ranges from -5% at the lowest altitudes to $\sim$ +2% above 200 km. The [O] uncertainty and error are below 10% above $\sim$175 km. The [O] random uncertainty increases with decreasing altitude, likely due to the decreasing relative O abundance with decreasing altitude. The [N_2] profiles have larger random uncertainty and systematic error, likely due to their lower relative abundance, in particular at altitudes where $n_{N2}(z_1)$ is determined. The [N_2] random uncertainty increases with increasing altitude as the relative N[$_2$] abundance decreases. The [O]/[N_2] systematic error is below 20% below 300 km, while the random uncertainty ranges from $\sim$ 20% to 30%. Note, the systematic error is a bias in the retrieval and, therefore, can be removed from the data by scaling the data by $1/(1-\epsilon_s(z))$, where $\epsilon_s(z)$ is the systematic error reported in Figure 3. The data described and reported in this paper and made publicly available have not removed the systematic error and it should be considered when interpreting these results.

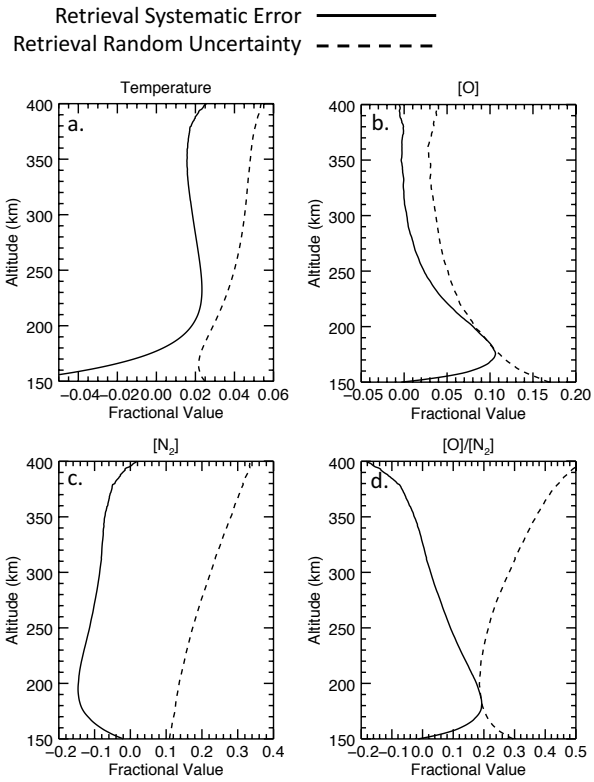

Figure 3. Random uncertainty and systematic error for the retrieved parameters. See text for details.

3 Results

Table 1. Coefficients for the temperature and abundance ratio data shown in Figures 4 - 7. Coefficients are found for each altitude and local time plotted. r is the Pearson correlation coefficient and $\frac{d}{EUV}$ is the sensitivity of the parameter to solar EUV irradiance (i.e. the fit slopes in the figures).

Parameter	Altitude	Dawn r	Dawn $\frac{d}{EUV}$	Dusk r	Dusk $\frac{d}{EUV}$
Temperature	170 km	0.71	66 K m^2/mW	0.82	69 K m^2/mW
Temperature	250 km	0.72	80 K m^2/mW	0.84	89 K m^2/mW
Temperature	350 km	0.69	92 K m^2/mW	0.84	97 K m^2/mW
[O]/[N_2]	170 km	0.13	0.24 m^2/mW	0.18	0.32 m^2/mW
[O]/[N_2]	250 km	0.08	0.38 m^2/mW	0.10	0.49 m^2/mW
[O]/[N_2]	350 km	0.033	-0.20 m^2/mW	0.032	0.81 m^2/mW
[O]=[N_2] Altitude	—	-0.42	-16 km-m^2/mW	-0.70	-27 km-m^2/mW
MSIS Temperature	170 km	0.94	62 K m^2/mW	0.93	73 K m^2/mW
MSIS Temperature	250 km	0.93	87 K m^2/mW	0.95	118 K m^2/mW
MSIS Temperature	350 km	0.92	93 K m^2/mW	0.95	138 K m^2/mW

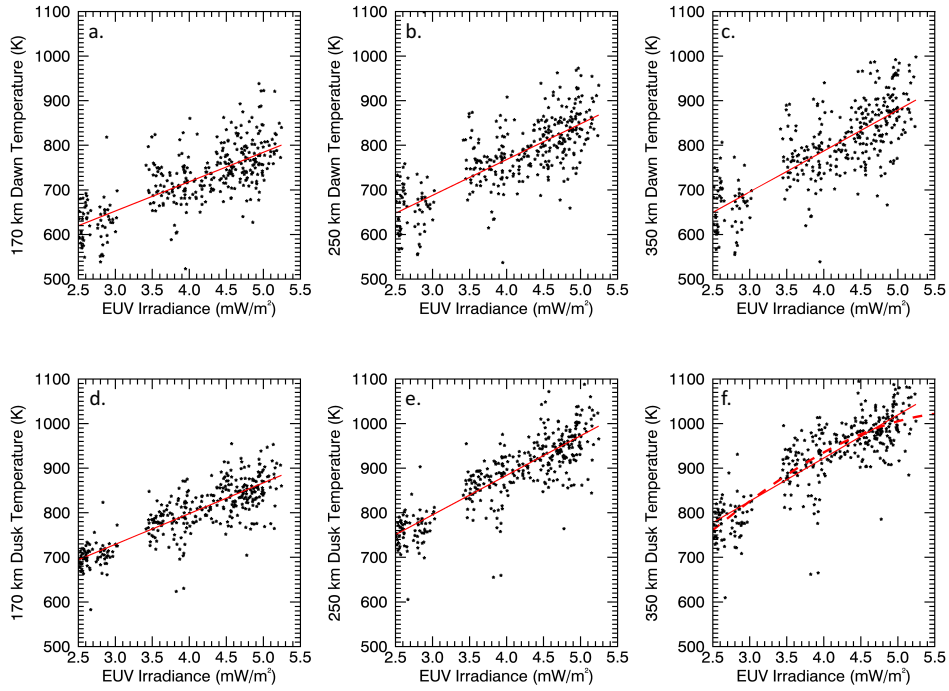

Figure 4. Relationship between thermospheric temperature and EUV irradiance at the dawn (top row) and dusk (bottom row) terminator at 170, 250 and 350 km.

The LYRA temperature and composition data are publicly available at https://proba2.sidc.be/data/lyra/OplusN2. In this section, we present an initial analysis that compares changes in temperature and composition to solar EUV irradiance and compares these results to the MSIS model as a proxy for prior measurements. Additionally, exospheric temperature sensitivities to EUV variability are derived and compared with similar measurements made at Mars.

Figure 4 shows how the observed thermospheric temperature varies with ionizing solar irradiance. Integrated 0-103 nm solar irradiances are computed from the Flare Irradiance Spectral Model 2 (FISM2; Chamberlin et al. (2020)) for days corresponding with the LYRA observations. Dawn and dusk temperature data are considered separately, and scatter plots of temperatures at 170 km, 250 km and 350 km are shown. Linear fits between temperature and irradiance are over-plotted in red. From Figures 4 e and f, the relationship between temperature and EUV irradiance appears somewhat non-linear, with the slope tending to flatten at higher irradiances. A red dashed line is plotted in panel f to guide the eye. This non-linearity indicates that the dusk terminator temperature becomes less sensitive to EUV irradiance either as it warms or as the irradiance intensity increases. For this paper, only coefficients from first-order linear fits are considered. Table 1 shows the Pearson correlation coefficients (r-values) and the fit slopes in the first three rows. These same parameters are calculated for MSIS temperature predictions at the same local times and altitudes, and are shown in the last three rows of Table 1.

Comparing the LYRA and MSIS coefficients, the MSIS r-values are higher than those from the observations, which is to be expected since MSIS does not include short time-

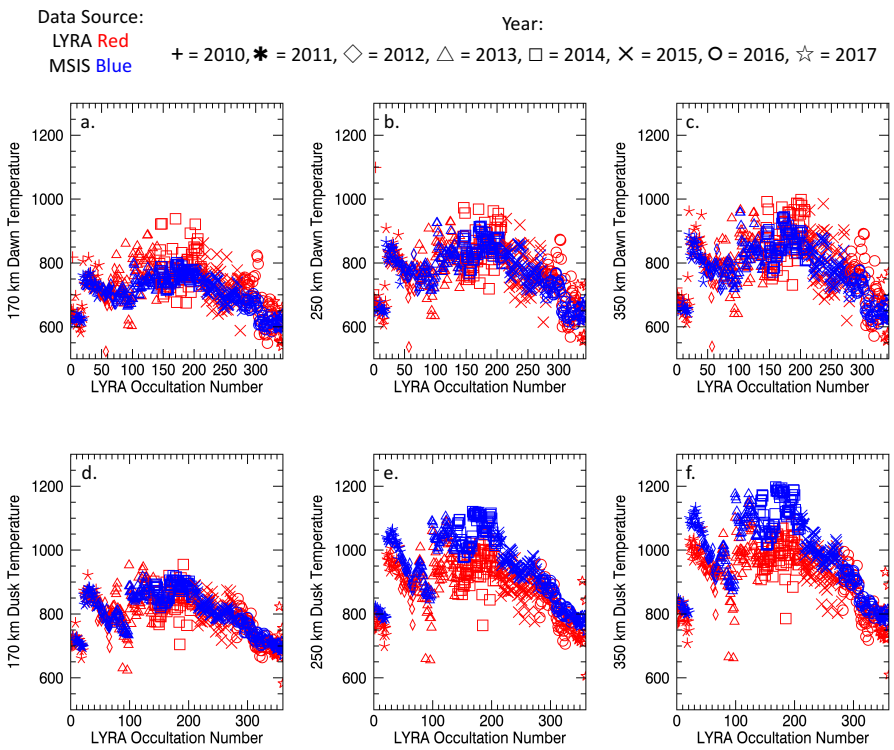

Figure 5. Comparison of LYRA measured (red) and MSIS modeled (blue) temperatures at the dawn (top row) and dusk (bottom row) terminator at 170, 250 and 350 km. The x-axis corresponds with observation number and are not continuous in time. The symbols distinguish the corresponding year as defined in the legend.

scale variability (e.g. wave activity and sub-daily solar and geomagnetic fluctuations). The dawn temperature EUV sensitivity (defined as the slope of temperature versus EUV irradiance, $dT/dEUV$) derived from the LYRA and MSIS data are comparable at the Dawn terminator, but markedly different at and above 250 km at the Dusk terminator. The LYRA and MSIS temperatures are compared directly in Figure 5, which confirms the results of Table 1, showing good agreement at the Dawn terminator but disagreement at the higher altitude Dusk terminator. The data plotted in Figure 5 begin in 2010 and end in 2017; see the legend at the top of the figure to identify individual years. The impression of the solar cycle is clear, with the warmest temperatures corresponding with solar maximum. Considering panels e and f, the LYRA temperatures tend to be cooler than those from MSIS, with the difference increasing with increasing solar activity.

The dependence of composition on solar EUV irradiance is shown in Figures 6 and 7. Figure 6 shows that the $[O]/[N_2]$ increases with increasing solar EUV irradiance at both dawn and dusk and all altitudes except for the highest Dawn altitudes. However, the correlations are much smaller than those between temperature and solar EUV irradiance. The fourth through sixth columns in Table 1 report the r-values and abundance EUV sensitivities (defined as the slope of $[O]/[N_2]$ versus EUV irradiance, $\frac{d[O]/[N_2]}{dEUV}$). Figure 7 shows the altitude where [O] equals $[N_2]$ versus solar EUV irradiance for Dawn and Dusk. Above this altitude, O is the dominant major species, while below, N_2 is the dominant major species. As solar activity increases, the altitude at which [O] becomes the

dominant species decreases. The corresponding slopes and r-values are reported in Table 1. It is notable that the correlation between the major species transition altitude and solar EUV irradiance is markedly higher than the correlation between [O]/[N_2] versus EUV irradiance at a fixed altitude.

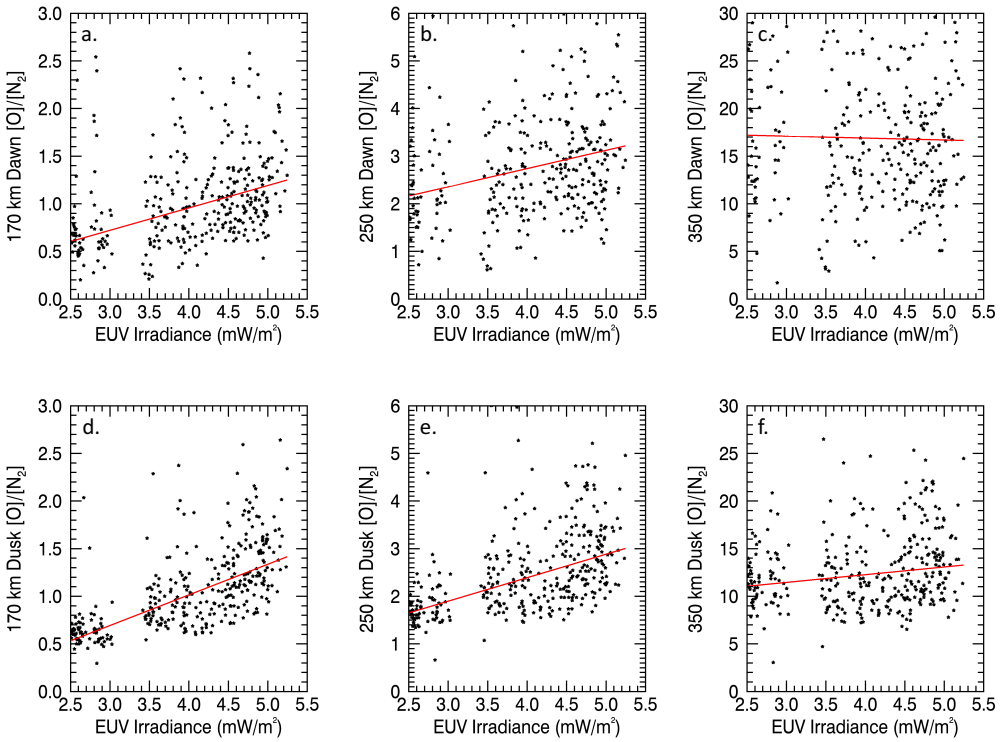

Figure 6. Relationship between [O]/[N_2] and EUV irradiance at the dawn (top row) and dusk (bottom row) terminator at 170, 250 and 350 km

4 Discussion

LYRA solar occultations provide observations of thermospheric temperature and major species (O and N_2) density and composition, made annually at the northern hemisphere from late-2010 through the present, spanning nearly an entire solar cycle. The longevity of the measurement and its inherent constancy in local-time lend these data to be particularly useful for examining long-term (weeks to years) trends in thermospheric variability. The random uncertainty of the temperature measurement is very low, $\sim$ 2-5%, while the [O] uncertainty is slightly higher. The [N_2] uncertainty exceeds 20% above 200 km as a result of its decreasing relative abundance making it increasingly difficult to distinguish it in the primary [O] + [N_2] measurement. These uncertainties are comparable to those reported for TIMED/GUVI limb scans in Meier et al. (2015), with the temperature uncertainties being approximately the same for both, and the [O] ([N_2]) uncertainties for LYRA being smaller (larger) than those for GUVI.

The physical relationship between solar EUV irradiance and thermospheric temperature is complex, beginning with photoionization or photodissociation of neutral constituents that ultimately heat the neutrals through multiple pathways. The primary pathway for neutral heating is through exothermic chemical reactions while heating through

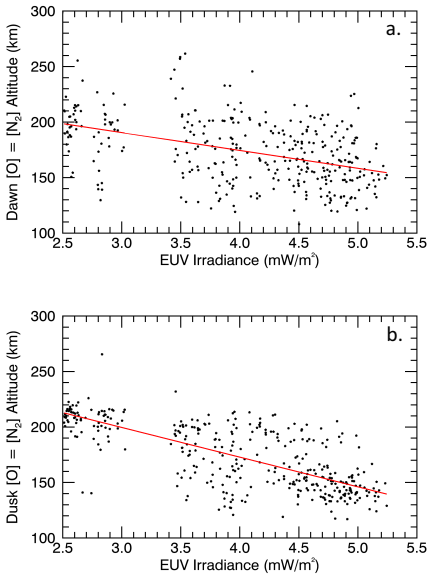

Figure 7. Altitude where [O] equals [N_2] versus EUV irradiance at the (a) dawn and (b) dusk terminators.

neutral collisions with electrons and ions plays a secondary role (Torr et al., 1980). This heat is then dissipated via downward thermal conduction and radiative cooling, with 5.3 μm NO emissions being the dominant radiative cooling pathway (R. Roble & Emery, 1983). The balance between heating and cooling along with the atmosphere's heat capacity determines the ultimate temperature of the thermosphere. Despite this complexity, these LYRA measurements show the relationship between temperature and ionizing solar EUV input is fairly linear, with a value of approximately 85 K-m^2/mW in the middle thermosphere at the terminator. A close examination of Figure 4 shows some non-linearity, with the slope of the relationship flattening at higher EUV irradiance values, an effect that is more pronounced at the high altitude dusk terminator. These results are consistent with the dependence of the MSIS global mean temperature on solar EUV input, which can be approximated as linear but has a negative inflection (e.g. see Figure 6 in A. Hedin and Mayr (1987)). More recent measurements using TIMED/GUVI between 2002 and 2008 showed a similar relationship between exospheric temperature and EUV flux (Y. Zhang & Paxton, 2011). The example non-linear fit in Figure 4f of this paper uses the form of Equation (2) from Y. Zhang and Paxton (2011).

The physical relationship between the relative O and N_2 abundance and solar EUV input can be explained by thermal expansion: Beginning with profiles for [O] and [N_2] of the approximate form,

$$[O(z)] = [O(z_0)] \exp\left(-\frac{m_O g(z)}{kT}(z - z_0)\right) \tag{6}$$

and

$$[N_2(z)] = [N_2(z_0)] \exp\left(-\frac{m_{N2} g(z)}{kT}(z - z_0)\right) \tag{7}$$

and setting [O(z)]=[N_2(z)], it is straightforward to show that the altitude where [O] equals [N_2] (and above which [O] > [N_2]) is dependent on temperature according to

$$z(O = N_2) = z_0 - \frac{k \ln\left([O(z_0)]/[N_2(z_0)]\right)}{g\,|m_{N2} - m_O|} T. \tag{8}$$

Since T has a fairly linear dependence on the solar EUV irradiance, as the solar EUV input increases, T increases, causing the altitude at which [O] equals [N_2] to decrease, consistent with Figure 7. A secondary result is the increase of [O]/[N_2] with EUV irradiance. Although Figure 6 shows [O]/[N_2] becomes less correlated with solar EUV irradiance at high altitudes, this may simply be a result of [O]/[N_2] becoming increasingly difficult to measure at high altitudes and the higher corresponding uncertainty could be masking the actual trend.

The comparisons between LYRA and MSIS show very good agreement at the dawn terminator but disagreement at the dusk terminator above 250 km. Because MSIS is an empirical model, comparisons with MSIS are effectively comparisons with the measurements against which MSIS has been calibrated. Considering first the dawn terminator, the mean differences at 170, 250 and 350 km are 21, 4, and 14 K (where a positive value indicates a warmer LYRA temperature) and the standard deviations are 51, 58, 69 K, respectively. These offsets and standard deviations are comparable with those between MSIS and the measurements used to calibrate MSIS reported in Table 2c of A. E. Hedin (1987). Since the atmosphere at the dawn terminator is representative of nightside conditions, given that it has co-rotated from the nightside shortly prior to being measured, these comparisons suggest that thermospheric variability over a solar cycle is well captured by the existing data record not only at the terminator but the nightside as well.

It is important to note that, while LYRA makes an independent measurement of T_{exo}, there may be some dependence of the LYRA temperature profiles on MSIS based on the constraints placed on the shape of the LYRA temperature profile. As discussed in Section 2, the values of a and τ in Equation 1 are forced to be within one standard deviation of the a and τ values predicted by MSIS for a given T_{exo}. Since the shape of the temperature profile is determined by a and τ, it is not surprising to find that if LYRA and MSIS have comparable temperatures at high altitudes, they also tend to agree at lower altitudes as is apparent at the dawn terminator. As is discussed next, the trends between LYRA and MSIS observed at the dusk terminator show that significantly differing values of T_{exo} between LYRA and MSIS can still result in better agreement at lower altitudes. Therefore, constraining a and τ to be consistent with MSIS still allows the temperature structure observed by LYRA to differ significantly from that predicted by MSIS.

The discrepancy at the dusk terminator between LYRA and MSIS, which increases with solar activity, is more difficult to explain. MSIS derives its temperatures at these altitudes from in-situ measurements made by the Atmospheric Explorer satellites flown in the 1970s and ground based incoherent scatter radar (ISR) measurements made from stations at Millstone Hill and Arecibo. The Atmospheric Explorer C-E probes measured atmospheric profiles of temperature early in their respective missions during, when their orbits were highly elliptical prior to being circularized at approximately 400 km to extend mission lifetime. The Atmospheric Explorer C-E probes measured temperature from 1973 to 1978 at a time when the solar cycle was in a trough of moderate to low levels of EUV intensity (the 90-day average F10.7 flux was below 100 SFU over this period). This under-sampling of in-situ measurements at higher solar EUV intensity could explain why the discrepancy between LYRA and MSIS at the dusk terminator is exacerbated near solar maximum. In other words, the available data at dusk local-times is inadequate to predict the flattening of the Temperature-Irradiance relation at higher solar irradiances. However, in-situ measurements are only one component of the MSIS data record.

The under-sampling of solar activity of the AE probes is compensated for with additional ISR measurements in the NRLMSISE-00 version of the model used in this study.

Neutral temperatures are derived from ISR ion temperature measurements by fitting a model of ion heat balance and chemistry to the measured ion temperature profile. The available ISR database used by NRLMSISE-00 is well-distributed in both local time and solar activity (Buonsanto & Pohlman, 1998). The retrieval of neutral temperature from ISR ion temperature measurements requires knowledge of the neutral density and composition, which is derived from the prior MSIS version, MSIS-86 (A. E. Hedin, 1987). We speculate that the complexity and underlying assumptions of the ISR temperature retrieval and its dependence on MSIS for neutral density and composition could contribute to the observed discrepancy. For example, it is unclear whether erroneous estimates of neutral density and composition by MSIS-86 at the terminator during high levels of solar activity causes the observed discrepancy between MSIS and LYRA. Fortunately, this hypothesis can be tested with ISR measurements that overlap with the past LYRA campaigns, if they exist, or planned future measurements if no adequate measurements exist in the historical archive. However, such an analysis is beyond the scope of this paper.

Some of the discrepancy between LYRA and MSIS can be attributed to an increase of relative CO_2 abundance during the LYRA epoch as compared to the epoch over which much of the MSIS calibration data were collected decades earlier. The thermosphere is expected to cool with increasing relative CO_2 abundance by 15μm radiation excited via collisions between O and CO_2 (R. Roble & Dickinson, 1989). Simulations predict that the expected change in diurnally averaged temperature at 350 km due to CO_2 cooling is approximately 11 K from 1977 to 2017 (Solomon et al., 2018) with CO_2 cooling being more pronounced near solar minimum (Qian et al., 2006). This has been supported by ISR observations showing a 4K/decade (or 16 K over 40 years) cooling trend at 350 km (S.-R. Zhang & Holt, 2013). Further, S.-R. Zhang and Holt (2013) showed that thermospheric CO_2 induced cooling is highly sensitive to local time with the temperature change at midnight at 350 km being near zero, while being nearly 80 K at noon at 350 km. They estimated that the CO_2 cooling rate measured at dusk at 350 km is $\sim$-0.5 K/year while the cooling rate measured at dawn is near 0 K/year. Indeed, the LYRA measurements in 2017, near solar minimum when CO_2 cooling is expected to be more pronounced, are consistent with what is expected from anthropogenic climate change, with the temperature change at dawn being 5 K cooler and that at dusk being 24 K cooler than MSIS estimates. It should be noted that because the NRLMSISE-00 T_{exo} measurements are derived from data ranging from the 1970s through the late 1990s, it is difficult to put a reference year on the data for characterizing long-term change. 1977 is chosen for simplicity to show qualitatively that anthropogenic cooling can cause some of the observed discrepancy.

The variation of the discrepancy with solar activity between LYRA and MSIS temperatures at the dusk terminator at 350 km are comparable in magnitude to those reported between GUVI and MSIS in Meier et al. (2015), but opposite in sign. Meier et al. (2015) reported the difference between MSIS predictions and GUVI measurements of T_{exo} decreased by $\sim$100 K with increasing solar activity from 2002 to 2007, while Figure 5f shows a $\sim$100 K *increase* in the difference between MSIS predictions and LYRA measurements of T_{exo} with increasing solar activity over a comparable period of solar activity occurring between 2013 and 2017. Since GUVI and LYRA observe different local times, with GUVI observing the dayside away from twilight, and LYRA observing exclusively at twilight, the different trends observed by GUVI and MSIS may be related to local times observed. The cause for the LYRA-MSIS discrepancy at the dusk terminator beyond what is expected from CO_2 cooling is under investigation. Since much steeper temperature gradients are expected at the dusk terminator than the dawn terminator in winter hemisphere (e.g. Bougher et al. (2000)), it may be that the MSIS-LYRA dis-

crepancy reflects that the MSIS data record does not have sufficient local-time resolution at the dusk terminator.

The LYRA mission overlaps in time with EUV solar occultations made at Mars by the Extreme Ultraviolet Monitor (EUVM) onboard the Mars Atmosphere and Volatile EvolutioN (MAVEN) mission, allowing for the comparison of EUV sensitivities measured at Earth and Mars at the same local times during similar, if not identical, levels of solar activity. Comparative modeling studies incorporating contemporaneously measured EUV sensitivities can help constrain the understanding of the thermal balance of the Mars thermosphere, which is less well understood than that of Earth (Forbes et al., 2006). Thiemann et al. (2018) reported values for dT/dEUV measured at Mars between 2014 and 2017 at various seasons and latitudes. Considering only cases for when the correlation r-value between temperature and solar EUV irradiance exceeds 0.7, the average values for dT/dEUV are 48 and 46 Km^2/mW at the dusk and dawn terminator, respectively, for exospheric temperatures. These values should be decreased by ∼5% prior to comparing with dT/dEUV values shown in Table 1 to account for a spectral range of 0-93 nm used by Thiemann et al. (2018) in their calculations, which is consistent with the range of ionizing flux in the CO_2 dominated Mars atmosphere. The Mars exospheric EUV sensitivities are calculated to be 0.47 of those found at Earth and reported in Table 1 , with the fraction being the same at both terminators. In other words, the Mars thermosphere is less sensitive to EUV forcing and requires twice the change of EUV irradiance as is required at Earth to induce the same change in temperature. This value is nearly identical to the Mars/Earth dT/dEUV fraction of 0.46 found by Forbes et al. (2006) during 2 periods of significant solar EUV modulation due to solar-rotations.

5 Conclusions

1. LYRA provides a new data record of thermospheric temperature and composition with adequate accuracy for characterizing long term trends in the thermosphere. Trends of temperature with EUV variability are approximately linear, with a decreasing slope at high levels of activity. This relation is consistent with prior measurements. Trends of composition measurements with EUV variability are consistent with thermal expansion of the diffusively separated thermosphere.

2. Thermospheric temperatures measured by LYRA are in good agreement with expectations based on the historical data record at the dawn terminator, but anomolously cool at the dusk terminator. Some of the disagreement at the dusk terminator, near periods of low solar activity in particular, is consistent with the expected cooling due to the anthropogenic increase of CO_2. However, the increase of the discrepancy with solar activity is not understood.

3. Comparing exospheric EUV temperature sensitivities at Earth and Mars show that Mars is 0.47 as sensitive to EUV variability as is Earth, this value is is excellent agreement with a prior estimate by Forbes et al. (2006).

Acknowledgments

Dr. Thiemann acknowledges Dr. Jeffrey Thayer of the University of Colorado for his helpful discussion regarding the applicability of the Bates temperature profile, and Dr. Matthew West of South West Research Institute for helpful discussions regarding the approach to the retrieval. Dr. Thiemann also acknowledges the PROBA2 Guest Investigator program for funding aspects of this project and providing technical support.

FISM-2 spectral irradiance data were downloaded from https://lasp.colorado.edu/lisird/ .

The Levenberg-Marquardt method was applied using mpfit.pro available through the IDL Astro library.

MSIS outputs were produced using the NRLMSISE-00 code available through the NASA Community Coordinated Modeling Center at
https://ccmc.gsfc.nasa.gov/pub/modelweb/atmospheric/msis/nrlmsise00/ .

Thermospheric temperature and composition are retrieved from the LYRA total number density profiles described in Thiemann et al. (2017) and publicly available on the web at https://proba2.sidc.be/data/lyra/OplusN2.

References

Aikin, A., Hedin, A., Kendig, D., & Drake, S. (1993). Thermospheric molecular oxygen measurements using the ultraviolet spectrometer on the solar maximum mission spacecraft. *Journal of Geophysical Research: Space Physics*, *98*(A10), 17607–17613.

Bates, D. R. (1959). Some problems concerning the terrestrial atmosphere above about the 100 km level. *Proceedings of the Royal Society of London. Series A. Mathematical and Physical Sciences*, *253*(1275), 451–462.

BenMoussa, A., Dammasch, I., Hochedez, J.-F., Schühle, U., Koller, S., Stockman, Y., ... others (2009). Pre-flight calibration of lyra, the solar vuv radiometer on board proba2. *Astronomy & Astrophysics*, *508*(2), 1085–1094.

BenMoussa, A., Gissot, S., Schühle, U., Del Zanna, G., Auchère, F., Mekaoui, S., ... others (2013). On-orbit degradation of solar instruments. *Solar Physics*, *288*(1), 389–434.

Bougher, S., Engel, S., Roble, R., & Foster, B. (2000). Comparative terrestrial planet thermospheres: 3. solar cycle variation of global structure and winds at solstices. *Journal of Geophysical Research: Planets*, *105*(E7), 17669–17692.

Bruinsma, S., & Biancale, R. (2003). Total densities derived from accelerometer data. *Journal of Spacecraft and Rockets*, *40*(2), 230–236.

Bruinsma, S., Doornbos, E., & Bowman, B. (2014). Validation of goce densities and evaluation of thermosphere models. *Advances in Space Research*, *54*(4), 576–585.

Buonsanto, M., & Pohlman, L. (1998). Climatology of neutral exospheric temperature above millstone hill. *Journal of Geophysical Research: Space Physics*, *103*(A10), 23381–23392.

Carignan, G., Block, B., Maurer, J., Hedin, A., Reber, C., & Spencer, N. (1981). The neutral mass spectrometer on dynamics explorer b. *SSI*, *5*, 429–441.

Chamberlin, P. C., Eparvier, F. G., Knoer, V., Leise, H., Pankratz, A., Snow, M., ... Woods, T. N. (2020). The flare irradiance spectral model-version 2 (fism2). *Space Weather*, *18*(12), e2020SW002588.

Forbes, J. M., Bruinsma, S., & Lemoine, F. G. (2006). Solar rotation effects on the thermospheres of mars and earth. *Science*, *312*(5778), 1366–1368.

Fuller-Rowell, T., Codrescu, M., Moffett, R., & Quegan, S. (1994). Response of the thermosphere and ionosphere to geomagnetic storms. *Journal of Geophysical Research: Space Physics*, *99*(A3), 3893–3914.

Hedin, A., & Mayr, H. (1987). Solar euv induced variations in the thermosphere. *Journal of Geophysical Research: Atmospheres*, *92*(D1), 869–875.

Hedin, A. E. (1987). Msis-86 thermospheric model. *Journal of Geophysical Research: Space Physics*, *92*(A5), 4649–4662.

Lumpe, J. D., Floyd, L. E., Herring, L. C., Gibson, S., & Lewis, B. (2007). Measurements of thermospheric molecular oxygen from the solar ultraviolet spectral irradiance monitor. *Journal of Geophysical Research: Atmospheres*, *112*(D16).

Mayr, H., & Volland, H. (1973). Magnetic storm characteristics of the thermosphere. *Journal of Geophysical Research*, *78*(13), 2251–2264.

Meier, R., Picone, J., Drob, D., Bishop, J., Emmert, J., Lean, J., ... others (2015). Remote sensing of earth's limb by timed/guvi: Retrieval of thermospheric composition and temperature. *Earth and Space Science*, *2*(1), 1–37.

Miyoshi, Y., Fujiwara, H., Jin, H., & Shinagawa, H. (2015). Impacts of sudden stratospheric warming on general circulation of the thermosphere. *Journal of Geophysical Research: Space Physics*, *120*(12), 10–897.

Nier, A., Potter, W., Hickman, D., & Mauersberger, K. (1973). The open-source neutral-mass spectrometer on atmosphere explorer-c,-d, and-e. *Radio Science*, *8*(4), 271–276.

Oberheide, J., Forbes, J., Zhang, X., & Bruinsma, S. (2011). Climatology of upward propagating diurnal and semidiurnal tides in the thermosphere. *Journal of Geophysical Research: Space Physics*, *116*(A11).

Picone, J., Hedin, A., Drob, D. P., & Aikin, A. (2002). Nrlmsise-00 empirical model of the atmosphere: Statistical comparisons and scientific issues. *Journal of Geophysical Research: Space Physics*, *107*(A12), SIA–15.

Press, W. H., Teukolsky, S. A., Vetterling, W. T., & Flannery, B. P. (2007). *Numerical recipes 3rd edition: The art of scientific computing.* Cambridge university press.

Qian, L., Roble, R. G., Solomon, S. C., & Kane, T. J. (2006). Calculated and observed climate change in the thermosphere, and a prediction for solar cycle 24. *Geophysical research letters*, *33*(23).

Roble, R., & Dickinson, R. (1989). How will changes in carbon dioxide and methane modify the mean structure of the mesosphere and thermosphere? *Geophysical Research Letters*, *16*(12), 1441–1444.

Roble, R., & Emery, B. (1983). On the global mean temperature of the thermosphere. *Planetary and Space Science*, *31*(6), 597–614.

Roble, R. G. (1995). Energetics of the mesosphere and thermosphere. *The Upper Mesosphere and Lower Thermosphere: A Review of Experiment and Theory, Geophys. Monogr. Ser*, *87*, 1–21.

Roble, R. G., & Hays, P. (1972). A technique for recovering the vertical number density profile of atmospheric gases from planetary occultation data. *Planetary and Space Science*, *20*(10), 1727–1744.

Roble, R. G., Ridley, E., & Dickinson, R. (1987). On the global mean structure of the thermosphere. *Journal of Geophysical Research: Space Physics*, *92*(A8), 8745–8758.

Schunk, R., & Nagy, A. (2009). *Ionospheres: physics, plasma physics, and chemistry.* Cambridge university press.

Schunk, R., & Sojka, J. J. (1996). Ionosphere-thermosphere space weather issues. *Journal of Atmospheric and Terrestrial Physics*, *58*(14), 1527–1574.

Solomon, S. C., Liu, H.-L., Marsh, D. R., McInerney, J. M., Qian, L., & Vitt, F. M. (2018). Whole atmosphere simulation of anthropogenic climate change. *Geophysical Research Letters*, *45*(3), 1567–1576.

Sutton, E. K., Nerem, R. S., & Forbes, J. M. (2007). Density and winds in the thermosphere deduced from accelerometer data. *Journal of Spacecraft and Rockets*, *44*(6), 1210–1219.

Thiemann, E., Dominique, M., Pilinski, M., & Eparvier, F. (2017). Vertical thermospheric density profiles from euv solar occultations made by proba2 lyra for solar cycle 24. *Space Weather*, *15*(12), 1649–1660.

Thiemann, E., Eparvier, F., Bougher, S., Dominique, M., Andersson, L., Girazian, Z., ... Jakosky, B. (2018). Mars thermospheric variability revealed by maven euvm solar occultations: Structure at aphelion and perihelion and response to euv forcing. *Journal of Geophysical Research: Planets*, *123*(9), 2248–2269.

Torr, M. R., Richards, P., & Torr, D. (1980). A new determination of the ultraviolet heating efficiency of the thermosphere. *Journal of Geophysical Research: Space Physics*, *85*(A12), 6819–6826.

Vadas, S. L. (2007). Horizontal and vertical propagation and dissipation of gravity waves in the thermosphere from lower atmospheric and thermospheric sources. *Journal of Geophysical Research: Space Physics*, *112*(A6).

Wang, W., Lei, J., Burns, A. G., Solomon, S. C., Wiltberger, M., Xu, J., ... Coster, A. (2010). Ionospheric response to the initial phase of geomagnetic storms: Common features. *Journal of Geophysical Research: Space Physics*, *115*(A7).

Xu, J., Liu, H.-L., Yuan, W., Smith, A., Roble, R., Mertens, C., ... Mlynczak, M. (2007). Mesopause structure from thermosphere, ionosphere, mesosphere, energetics, and dynamics (timed)/sounding of the atmosphere using broadband emission radiometry (saber) observations. *Journal of Geophysical Research: Atmospheres*, *112*(D9).

Yiğit, E., & Medvedev, A. S. (2009). Heating and cooling of the thermosphere by internal gravity waves. *Geophysical Research Letters*, *36*(14).

Zhang, S.-R., & Holt, J. M. (2013). Long-term ionospheric cooling: Dependency on local time, season, solar activity, and geomagnetic activity. *Journal of Geophysical Research: Space Physics*, *118*(6), 3719–3730.

Zhang, Y., & Paxton, L. J. (2011). Long-term variation in the thermosphere: Timed/guvi observations. *Journal of Geophysical Research: Space Physics*, *116*(A2).